CHAPTER III

EXPERIMENTAL APPROACH

Experimental work was performed to verify the initial idea of using a spiral post-tensioning system for creating an active confined pressure. The work also demonstrated that a spiral post-tensioning system can be applied in realistic construction practices. A preliminary analysis of the series of specimens was prepared to estimate the capacity of specimens by assuming a confined concrete model and applying a finite difference method to analyze the strength of specimens. Additional details are subsequently illustrated in the analytical approach section.

Laboratory tests did not represent direct response of active confinement by using spiral post-tensioning system. These tests indirectly represented an active confinement behavior through bending behavior. Due to the limitation of specimen size and loading equipment, direct axial compression tests on concrete cylinders were not performed. Consequently, simple mid-span point loading tests were performed on thick-walled spirally post-tensioned specimens simply supported at their ends. In this way, the effect of active confinement on shear strength enhancement was experimentally investigated.

3.1 Test Program

Three spirally prestressed concrete cylinders were simply supported at their ends and tested to study their strength and behavior under mid-span loading. Each specimen had four clockwise and four counterclockwise post-tensioning strands each making a complete revolution from one end of a specimen to the other. Results were compared to those of a nominally identical control specimen consisting of a similar concrete cylinder with the same number of longitudinally aligned post-tensioning strands. The specimens were designed to study the effect of: (1) the

orientation of prestressing strands namely, spiral vs. straight, and; (2) the percentage magnitude of applied strand prestressing force namely, 25, 50, and 75 percent of the strand capacity for spirally configured specimens, and 50 percent for the control specimen with longitudinally aligned strands.
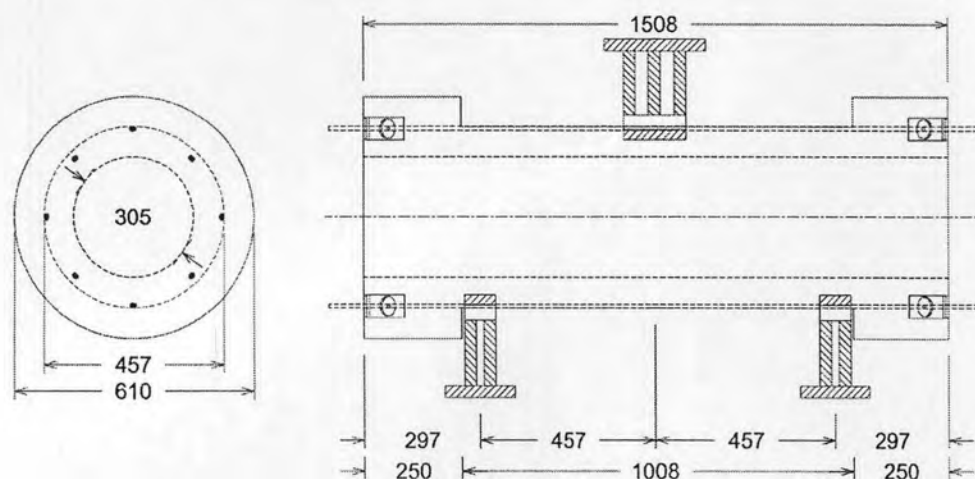

Figure 3.1 Specimen dimensions (in mm.)

Table 3.1 Specimen series

Series	%P/S	Orientation
H1	25	spiral
H2	50	spiral
H3	75	spiral
HC1	50	straight

3.2 Test Specimens

Referring to Figure 3.1, the test section of each specimen consisted of a concrete cylinder with a 457.2 mm (18 in.) outside diameter, a 304.8 mm (12 in.) inside diameter, and a wall thickness of 76.2 mm (3 in.) Four counter-spiraled pairs of 12.5 mm (0.5 in.) diameter prestressing strands were used. Thus, for specimens H1, H2, and H3, strands were oriented in a spiral configuration with four in the

clockwise and four in the counter-clockwise direction. Eight parallel strands aligned in the longitudinal direction were used for comparison specimen HC1. Self-consolidating concrete with a maximum aggregate size of 10 mm (3/8 in.) and an ultimate compressive strength of 58.6 MPa (8.5 ksi) was used for all specimens. A 250 mm (9.8 in.) long and 152.4 mm (6 in.) thick flanged extension anchorage zone, monolithically cast with the test section, was formed at the ends of each test specimen. These flanges were used to hold the end anchorage devices. All post-tensioning was accomplished using the DSI-America Monostrand® post-tensioning system grade 270 low-relaxation. Each tendon in this system is pre-equipped with a snugly fitting flexible duct that facilitates construction and post-tensioning procedures.
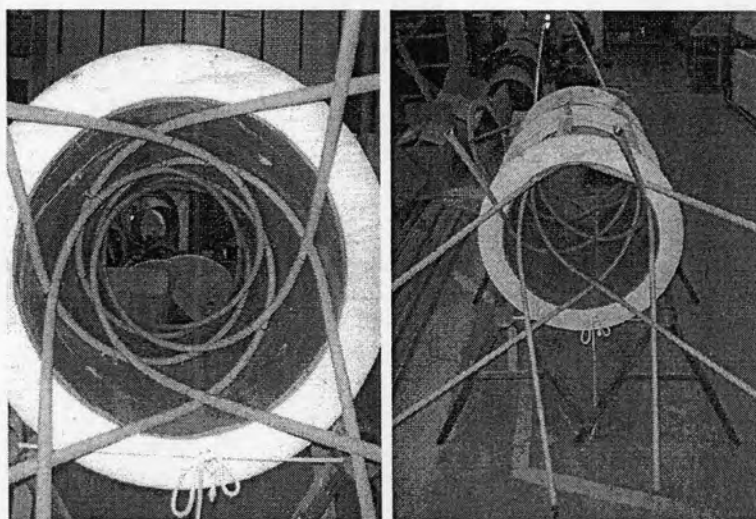

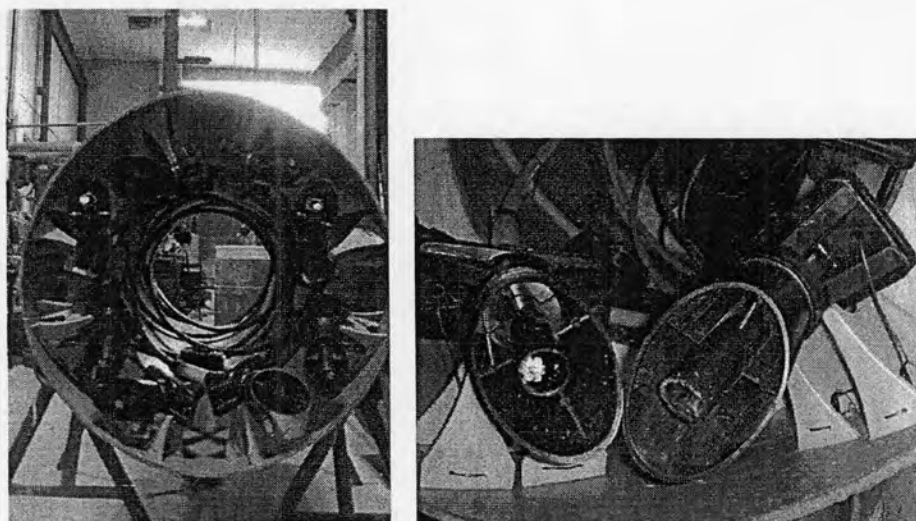Figure 3.2 Fabrication – Monostrand® Installed in the mold

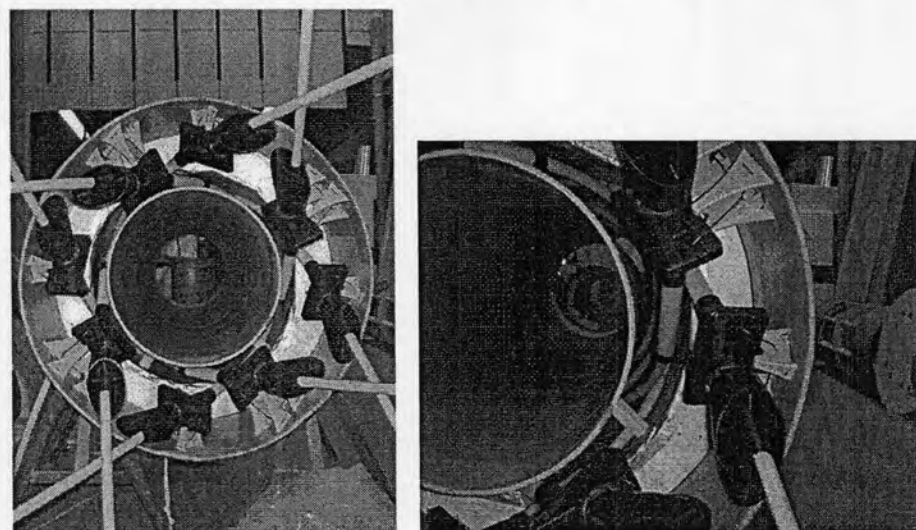Figure 3.3 Fabrication – Installed anchorage devices

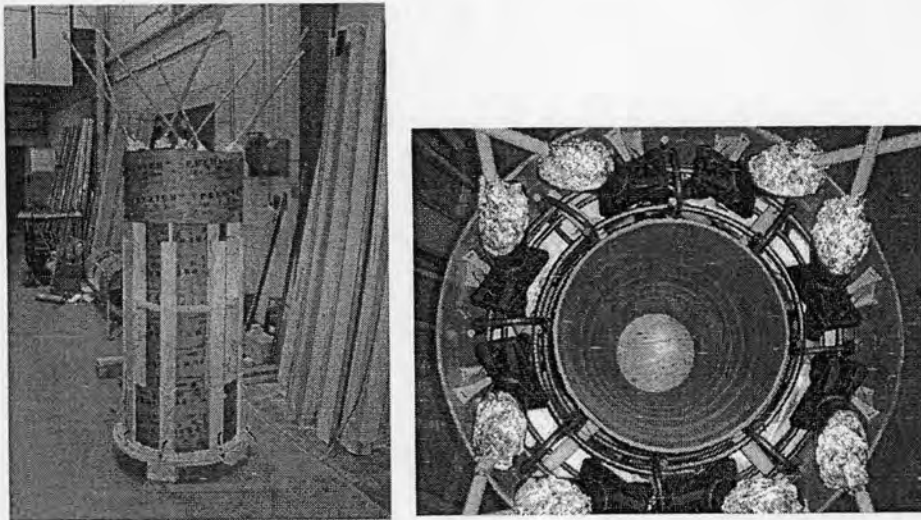Figure 3.4 Fabrication – Inner core mold inserted

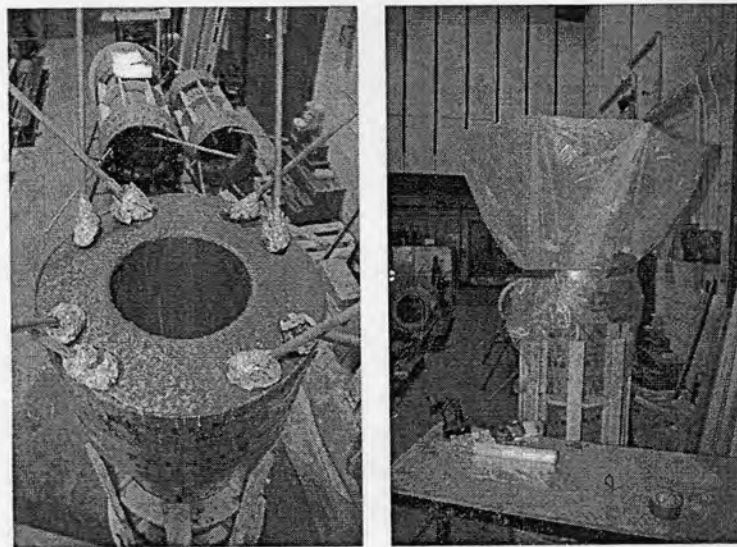Figure 3.5 Tilted up and ready to pour concrete

Figure 3.6 Pouring and curing

The results of standard compression cylinder tests are shown in Figure 3.7 while Table 3.2 shows the results of cylinder splitting tests and rupture tests of small beams.

Table 3.2 Splitting and beam tension tests

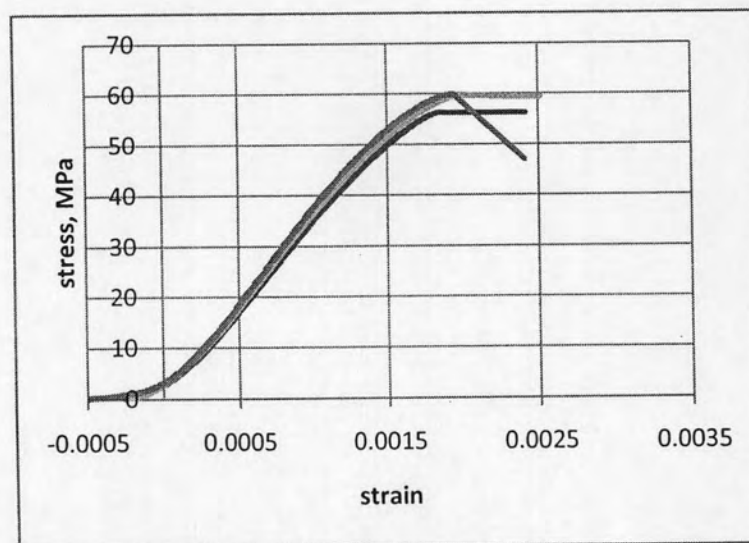|		Average
Splitting tensile strength, MPa	5.7	5.8
	5.7	
	5.9	
Flexural beam test, MPa	7.5	7.6
	7.8	
	7.5	

Figure 3.7 Cylinder compression test

3.2.1 Percentage of Prestressing Force

In order to study the effect of confining forces as a function of prestress levels, prestressing forces in specimens H1, H2, and H3 were applied at 25, 50, and 75 percent of the pulling strength of the Monostrand® grade 270 low relaxation. These values are also summarized in Table 3.3 below.

Table 3.3 Summary of prestress forces

Series	$\% P/s$	f_a/f_c' (%)	f_l/f_c' (%)	Orientation
H1	25	6.11	3.55	spiral
H2	50	12.61	7.33	spiral
H3	75	16.02	9.32	spiral
HC1	50	12.31	-	straight

3.2.2 Orientation of Prestressing Strands

Of the four tested specimens, H1, H2, and H3 had four pairs of counterbalancing spiraled strands while, for comparison, specimen HC1 had eight identical but parallel and longitudinally aligned strands. Each of the eight strands in specimens H2 and HC1 was prestressed to 50 percent of the tension strength of the strands. This provided an opportunity for direct evaluation of the strength and behavior of spiral prestressing as compared with standard longitudinally aligned prestressed strands.

3.2.3 Stressing Method, Loading Method, and Instrumentation

Using an overhead crane, each specimen weighing approximately 4.7 kN (1.0 kips.) was carefully set in place in the testing frame and instrumented with surface-mounted strain gauges while electronically monitored potentiometers were used to measure deflections. Specimens were then prestressed in place before testing proceeded. As indicated in Figure 3.8, a strict order of sequential post-tensioning was essential in avoiding torsional-bending failure during prestressing. This procedure included applying prestress simultaneously to counterbalancing pairs of clockwise versus counter-clockwise strands. Furthermore, stressing proceeded in increments $0.25f_{pu}$ completing all strands before proceeding with a higher increment in order to maintain unbalanced forces at an acceptable level. The records of stressing sequence are shown in Table 3.4.
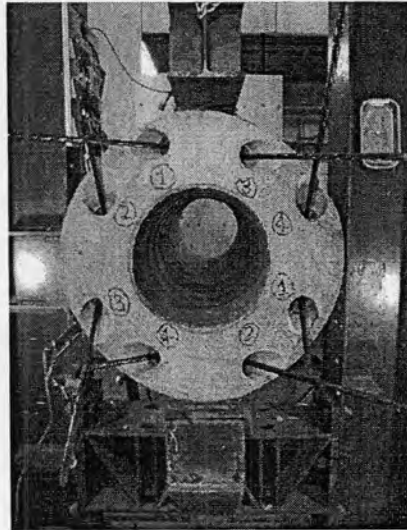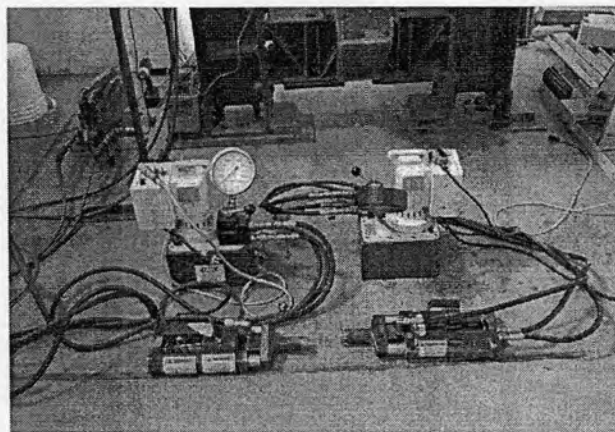
Figure 3.8 Post-tensioning number sequence
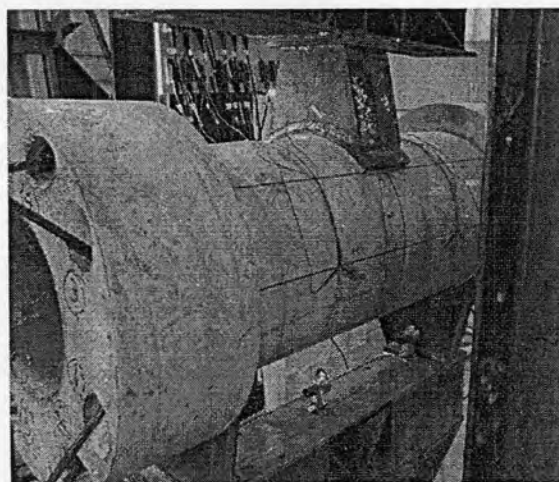

Figure 3.9 Twin ram jacks

Figure 3.10 Loading frame and Instrumentation

Table 3.4 Stressing records

Specimen:		H1		Specimen:		H2	
Jacking force:		13.1	kips	Jacking force:		26.2	kips
Gauge Pressure:		2079	psi	Gauge Pressure:		4157	psi
Tendon no.	Jacking Location	Gauge Reading	Jacking force	Tendon no.	Jacking Location	Gauge Reading	Jacking force
1	F	2100	13.2	1	F	4100	25.8
1	B	2100	13.2	1	B	4130	26.0
2	F	2100	13.2	2	F	4160	26.2
2	B	2100	13.2	2	B	4180	26.3
3	F	2100	13.2	3	F	4120	26.0
3	B	2100	13.2	3	B	4110	25.9
4	F	2100	13.2	4	F	4130	26.0
4	B	2100	13.2	4	B	4200	26.5

Specimen:		H3		Specimen:		HC1	
Jacking force:		33.4	kips	Jacking force:		20.7	kips
Gauge Pressure:		5299	psi	Gauge Pressure:		3284	psi
Tendon no.	Jacking Location	Gauge Reading	Jacking force	Tendon no.	Jacking Location	Gauge Reading	Jacking force
1	F	5300	33.4	1	F	3200	20.2
1	B	5300	33.4	1	B	3200	20.2
2	F	5300	33.4	2	F	3200	20.2
2	B	5300	33.4	2	B	3200	20.2
3	F	5300	33.4	3	F	3200	20.2
3	B	5290	33.3	3	B	3200	20.2
4	F	5300	33.4	4	F	3200	20.2

Referring to Figure 3.10, loading was performed in a specially designed self-equilibrating testing frame with a 1000 kN (225 kips.) capacity hydraulic load actuator. Load was applied at a deliberately slow rate to simulate static loading.

Carefully calibrated potentiometers were used to measure deflections at the bottom of each specimen. Surface-mounted rosette strain gauges were attached to measure stresses and principal directions in the concrete. All measuring instruments were connected to a high speed data acquisition system for simultaneous data collection in real time.
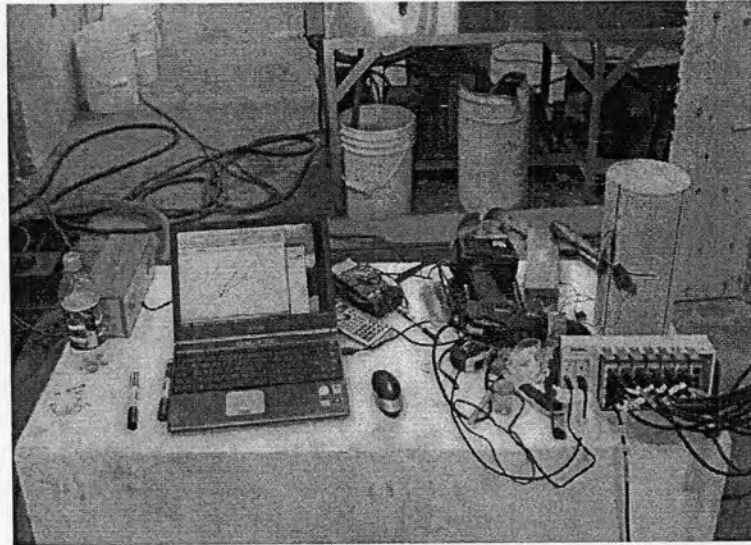

Figure 3.11 Data acquisition (DAQ)

3.3 Experimental results

Response of each specimen was used to interpret and clarify unexpected results. Measured prestress loss due to friction was assessed by using a twin ram jack as anchorage at the end of a specimen while applying prestress using a second twin ram jack at the opposite end. The difference in readings between pressure values from both pressure gauges on each hydraulic pump resulted in an indication of prestress loss due to friction.

Table 3.5 Measurement of friction loss

Gauge read on jack end (psi)	Force on jack end (tons)	Gauge read on Dead end (psi)	Force on dead end (tons)	%loss
1,600	4.6	1,100	3.1	32.6%
3,250	9.3	2,450	7.0	24.7%
3,700 (failed)	10.6	N/A	-	-
			Average	28.7%

From DSI Monostrand® properties, $\alpha_f = 0.07$, $k_f = 0.004$ $^1/_m$. Losses due to friction can be calculated as illustrated in equation (2.7). The value of friction loss from calculation (28.5%) compared very well with the measured value (28.7%) representing an almost negligible difference.

Since pressure gauges reached 3,700 psi (10.6 tons of jacking force), specimen suddenly failed along a strand alignment as shown in Figure 3.12. From the crack pattern, it appeared that specimen failed by unbalanced torsional force due to single strand tensioning combined with shear force from strands cutting through the concrete.
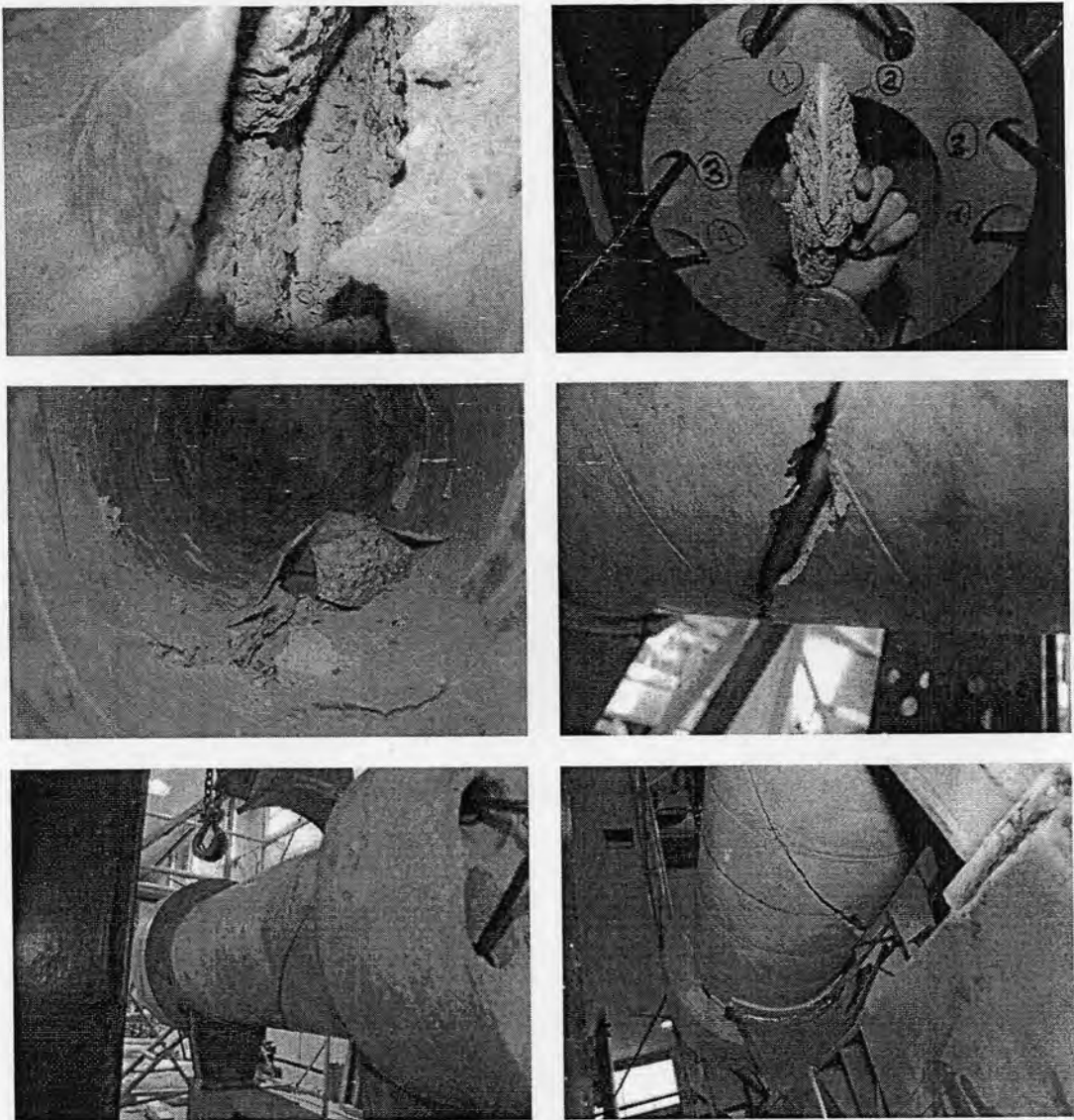
Figure 3.12 Specimen failure precipitated by concrete shearing stress in 1 strand

Following this action, 25% of pulling strength was exerted on the other strands in correct sequence to close the cracks to some extent. The specimen was thus partially repaired and ready to test on mid-span loading. The result is illustrated in Figure 3.13. Although the specimen had already failed, it was able to resist load and to show elastic behavior from the beginning until loading reached 15 tons. The ultimate strength was 18.85 tons. Compared to the capacity of specimen H1 with an ultimate strength of 39.83 tons and at the same level of prestressing it was apparent that a prototype specimen strength can be recovered up to almost 50% by using a spiral prestressing configuration as investigated in this dissertation.
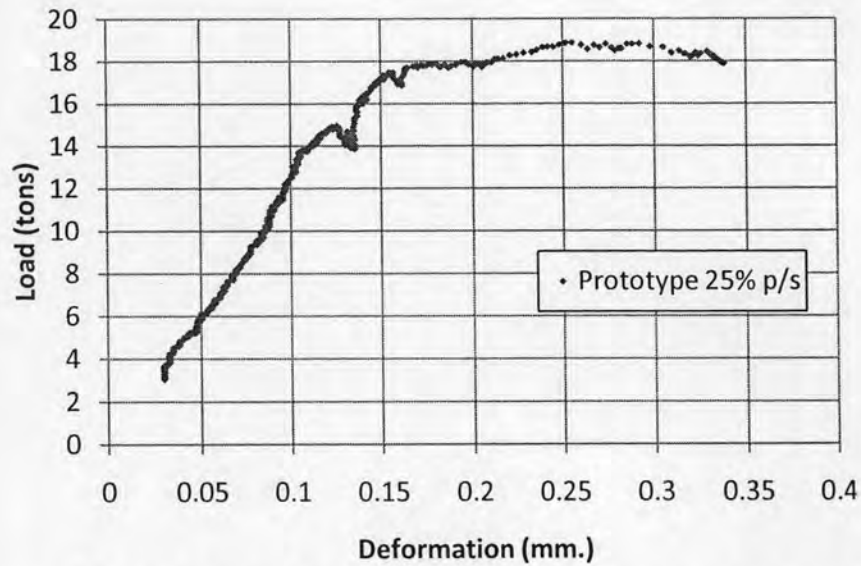
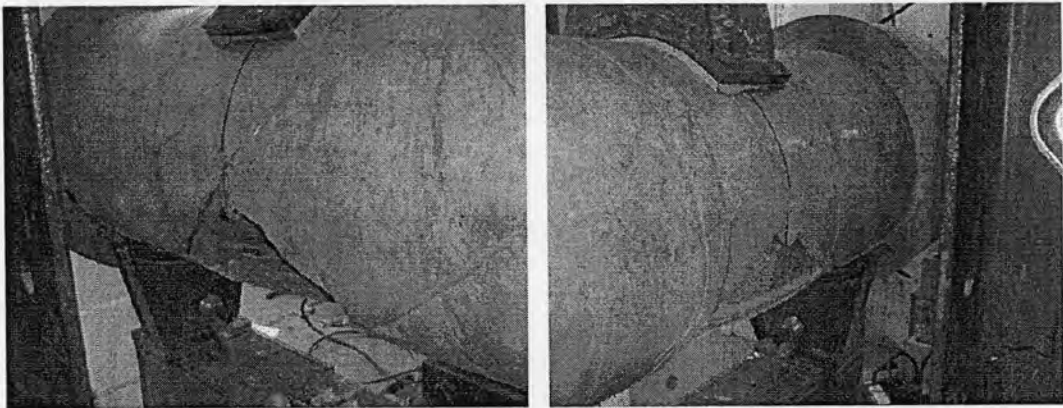Figure 3.13 Load vs. deformation curve of prototype specimen


Figure 3.14 Prototype specimen after loading

The behavior of the concrete cylinders, as subjected to three-point loading which induces bending moment and shear stresses, may be characterized by a load vs. deflection or $P - \delta$ curve, load vs. longitudinal strain at bottom of mid-span or $P - \varepsilon$ curve, and strain vs. deflection or $\varepsilon - \delta$ curve. The $P - \delta$ curves, $P - \varepsilon$ curves, and $\varepsilon - \delta$ curves for specimens H1, H2, H3, and HC1 are shown in Figure 3.15. All specimens firstly cracked by bending stress near mid-span at the bottom. Consequently, specimens formed arch action to transfer load from loading point to supports. Shear cracking were growth and shear behavior was taking a major effect to a deformation. All specimens suddenly failed by strands cutting through concrete

except specimen HC1 that diagonal cracks were connected and suddenly failed by diagonal shear failure.
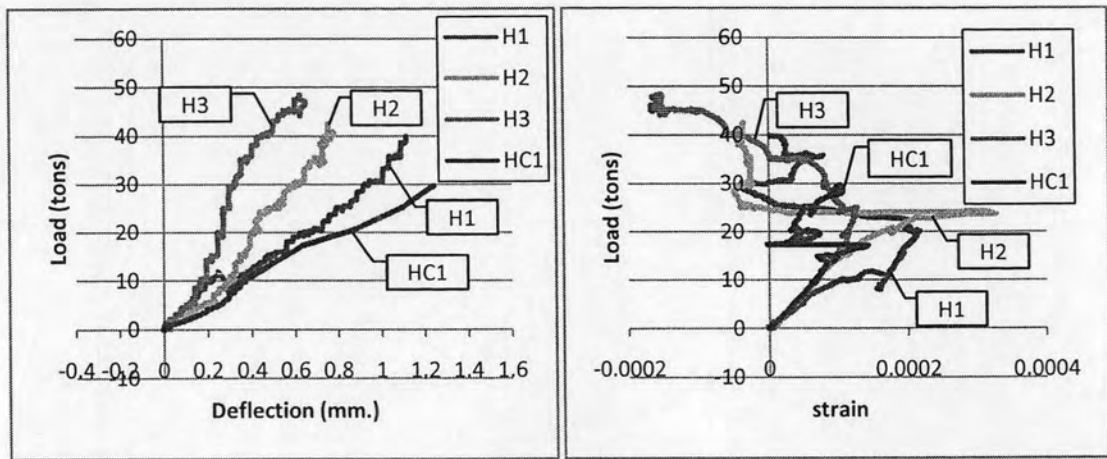
(a)

(b)
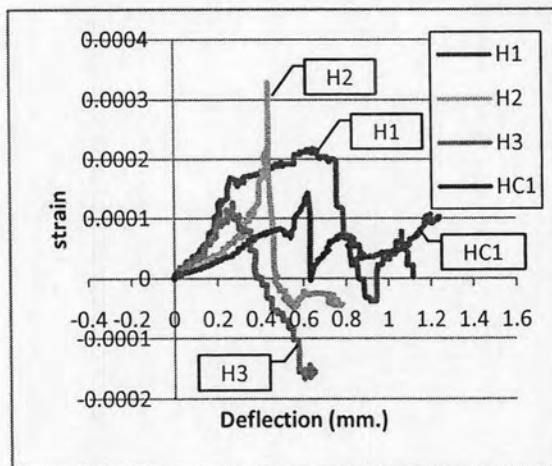
(c)

Figure 3.15 (a) Load vs. deflection curves, (b) load vs. longitudinal strain curves at bottom of specimen, and (c) longitudinal strain vs. deflection curves

Table 3.6 Summary of test results

Spec.	Stiffness (tons/m)	Cracking Load (tons)	Ultimate Capacity (tons)	Calc'd. Ultimate Capacity (tons)	Defln. at Ultimate (mm)	%P/s
H1	71,295	11.80	39.83	46.59	1.04	25%
H2	71,061	24.34	43.49	63.78	0.65	50%
H3	112,104	35.00	48.36	85.35	0.57	75%
HC1	40,590	17.27	29.72	57.04	1.04	50%

For the four specimens, these curves may be used to observe and compare cracking strength, stiffness, ultimate strength, and ductility as relations of prestress magnitude and strand configuration.

3.3.1 Cracking Strength

Cracking was detected visually and was also detected by rosette strain gauges placed at the bottom of each specimen caused by flexural stress and placed at mid-shear span of each specimen caused by diagonal shear stress. First crack of specimen H1 was very large as a result of low level of prestressing caused large strength decreasing portion and the traces of H1 and H2 appear to cross at approximately 10 tons. Figure 3.18 gives a summary of test findings for all specimens and shows that the crack load increases with increasing levels of prestress. According to Figure 3.15, the slippage of the curves shown gross faulting from adjustment of strands contact and from $P - \varepsilon$ curve, large slip of strain shown crack occurring and growth related to load increasing.

Flexural cracking strength can be determined by strain compatibility and diagonal shear cracking strength can be determined by combined stress analysis as shown in Figure 3.16 and Figure 3.17. The analysis results of cracking strength were shown in Table 3.7.
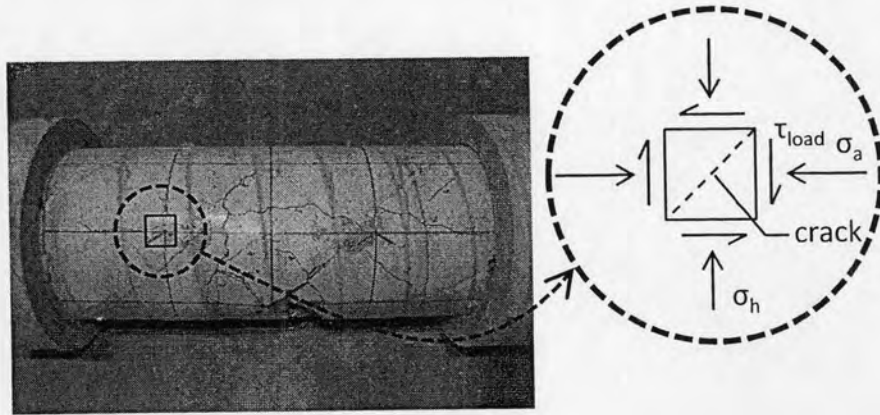
Figure 3.16 State of stresses of diagonal shear cracking

Horizontal shear tress from load, τ_{load} and maximum shear stress, τ_{max} can be expressed as shown below:

$$\tau_{max} = \frac{VQ}{Ib} \tag{3.1}$$

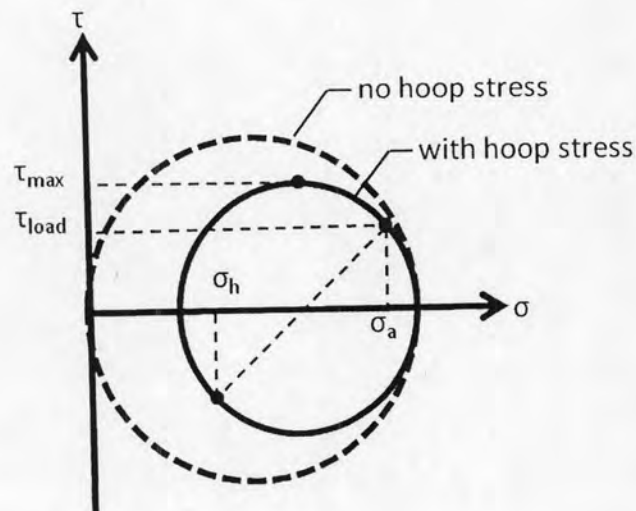$$\tau_{load} = \sqrt{\left(\frac{\sigma_a - \sigma_h}{2}\right)^2 + \tau_{max}^2} \tag{3.2}$$

Figure 3.17 Hoop stress effect represented by Mohr's circle

According to Table 3.7, cracking of all specimens can be detected by rosette strain gage. First crack was detected at mid-shear span caused by diagonal shear stress excepted specimen H1 that cracked by flexural stress. The calculated values of cracking load from combined stress analysis, $P_{cr2}^{cal.}$ are corresponding to the test results, P_{cr2}^{test}. And critical stress, τ_{max}^{test} are corresponding to spitting tensile strength

of concrete, $f_r^{splitting test}$=59 ksc. The increasing in cracking strength of diagonal shear cracking depends on the proportion of an axial stress to a hoop stress, $(\sigma_a - \sigma_h)$.

Table 3.7 Summary of cracking load

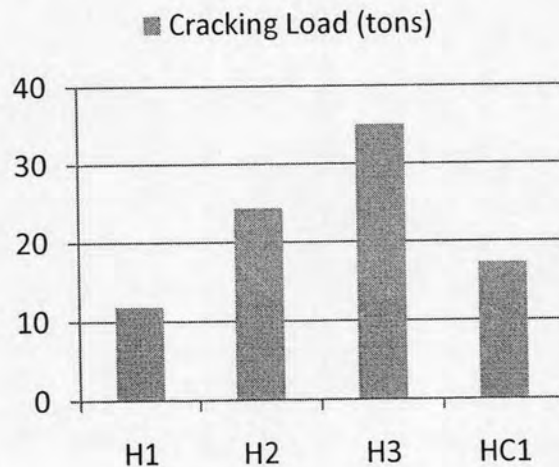| Series	Flexural cracking		Diagonal shear cracking			
	P_{cr1}^{test}, tons	$P_{cr1}^{cal.}$, tons	P_{cr2}^{test}, tons	τ_{load}, ksc	τ_{max}^{test}, ksc	$P_{cr2}^{cal.}$, tons
H1	11.80	24.78	22.47	65.22	65.26	20.31
H2	22.91	30.64	20.85	60.52	60.71	20.26
H3	24.99	36.51	22.55	65.45	65.85	20.17
HC1	17.27	38.82	15.17	25.07	48.11	17.09

Figure 3.18 Cracking strength

3.3.2 Stiffness

The stiffness at the initial portion (load approximately least than 5 tons) are slightly lower than following portion because of bedded material take-up. The deformation of bedded material was combined into the measured deformation. The measured deformation was corrected and illustrated in Figure 3.25. After concrete

already cracked by bending stress, arch action takes an effect and shear cracking induce shear deformation that reduce stiffness of specimen. The increase in stiffness of the specimens is related to confining stresses from prestressing force. The confining stresses or in another mean; hoop stress, σ_h and axial stress, σ_a, can control crack width from shear cracking action as shown in Figure 3.16, the resultant stress of prestressing force against crack direction.
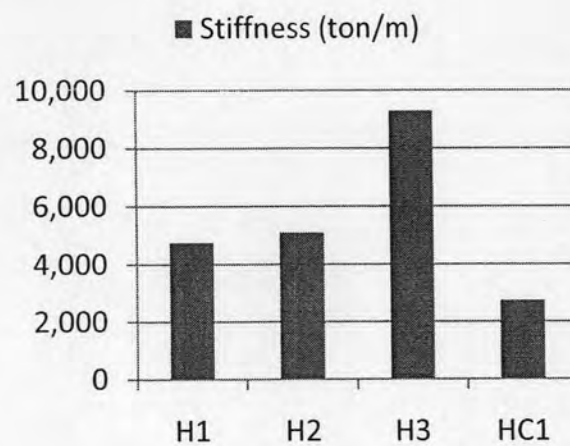

Figure 3.19 Stiffness

3.3.3 Ultimate Strength

As benefitted by the active confinement effect of a spiral post-tensioning system, referring to Figure 3.25, the ultimate strength of specimens H1, H2, and H3 in bending increased proportionally with increased levels of prestressing force. Additionally, the benefit of using a spiral post-tensioning system as in specimen H2 over the use of straight strand prestressing at the same level of prestressing force as in specimen HC1 is seen by comparing their respective ultimate capacities. In fact, the use of a spiral post-tensioning system at the same prestress level increases the ultimate strength of H2 by 45% over that of HC1 which had a straight configuration of tendons.

The ultimate capacity of specimens can be explain by bending theory, shear theory and arch action. According to bending theory, the ultimate capacity of specimen increases with increasing of longitudinal prestressing force as a pre-

compressive stress that will compensate with tensile stress from load. As shown in Table 3.6, the ultimate capacity from finite difference method (FDM) that base on bending theory with assumed confined concrete model, shown that the results were slightly lower than calculated results from FEM that can represent shear effect and arch action except the result of specimen HC1 from FEM that close to the test result. For three spiral reinforced specimens – H1, H2, and H3, the results from FEM are greater than the corresponding test values with the ratios of calculated to test values being 1.45, 1.67, and 1.79, respectively. According to the experimental investigation, three spiral reinforced specimens locally failed by strand cutting through concrete. Spiral reinforced specimens could not reach overall failure as predicted.
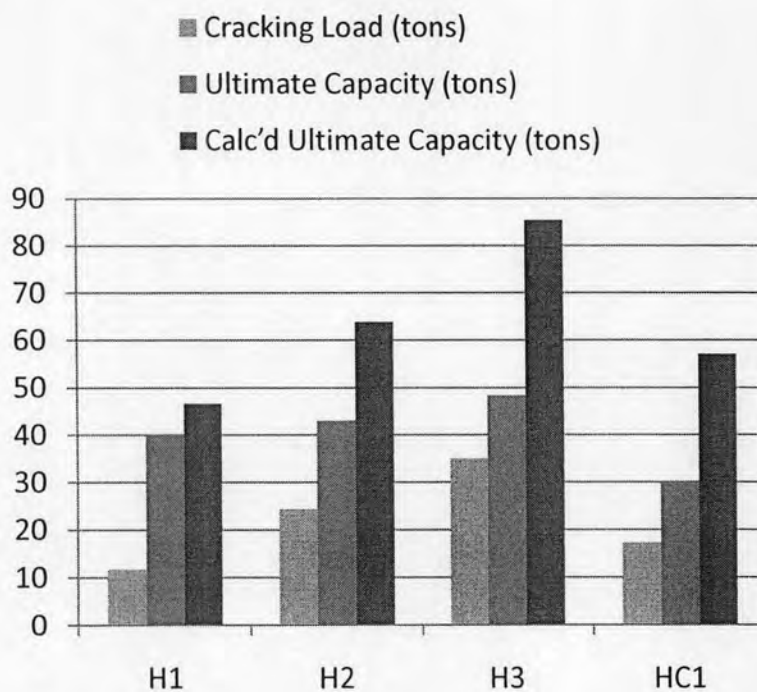

Figure 3.20 Cracking load, ultimate capacity and calculated ultimate capacity

The local failure by strand cutting through concrete can be determined by direct shear strength of concrete under axial loaded as shown in Figure 3.21 and can be calculated as expressed below:

for axial compression: $\quad v_c = 1.06 \left(1 + 0.0071 \frac{N_u}{A_g}\right) \sqrt{f_c'} t$ $\qquad$ (3.3)

for axial tension: $\quad v_c = 1.06 \left(1 + 0.029 \frac{N_u}{A_g}\right) \sqrt{f_c'} t$ $\qquad$ (3.4)

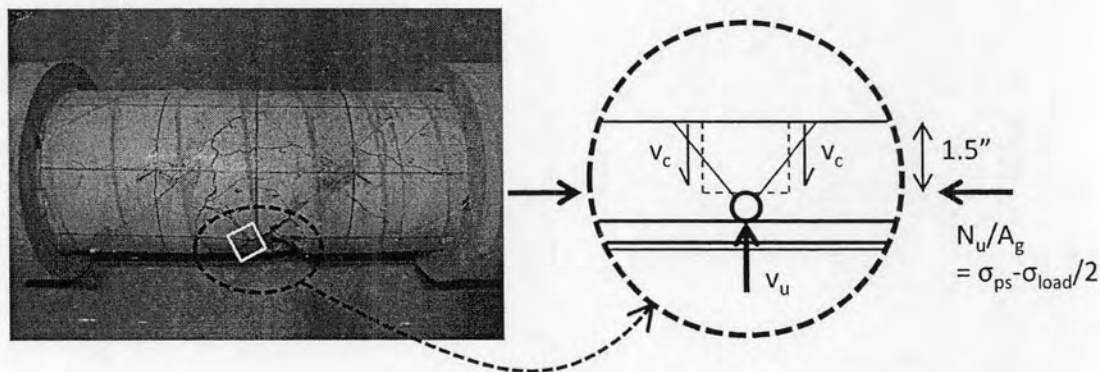$$\sigma_{ps} = \frac{(\sigma_h + \sigma_a)}{2} \tag{3.5}$$

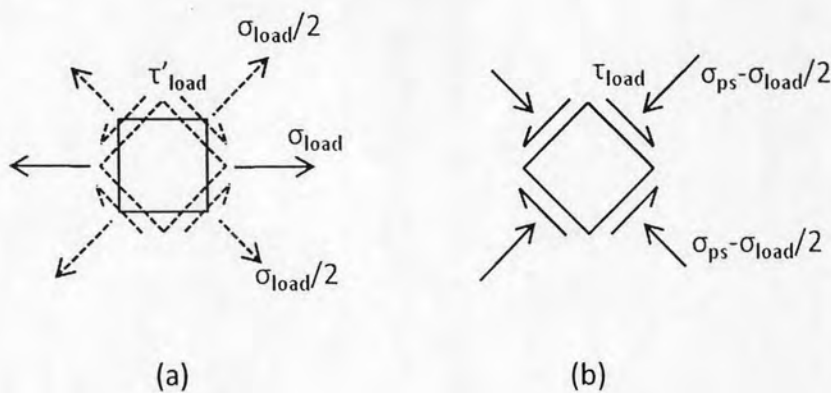Figure 3.21 Schematic of strand cutting through concrete

(a)

(b)

Figure 3.22 Superimpose of a) transformed flexural stress at bottom of specimen to b) combined stress on strand direction

According to Table 3.8, shear resistance capacity of concrete, v_c are corresponding to shear stress from strand, v_u. And calculated load resistance capacity of spiral specimens, $P_{cr3}^{cal.}$ are corresponding to failure load of spiral specimens, H1, H2, and H3.

Table 3.8 Summary of failure load due to strand cutting through concrete

Series	P_{cr3}^{test}	σ_{load}	σ_{ps}	N_u/A_g	v_c	v_u	$P_{cr3}^{cal.}$
H1	39.83	131.43	26.62	-39.10	24.67	25.60	31.61
H2	42.90	141.56	53.23	-17.55	48.46	51.19	42.32
H3	48.36	159.56	79.85	0.06	98.72	76.80	53.03

3.3.4 Ductility

This experimental investigation was designed to study the confining effect afforded by the spiral configuration of prestressing strands. Post-tensioning with end anchorage was used with no standard reinforcing steel present except that which was used to reinforce the pocket anchorage areas in the flanges which were outside of the actual specimen test length. The use of unbonded strands and the omission of standard steel reinforcement ensured the absence of any extraneous or random effects in pinpointing the clear beneficial effects of using a spiral post-tensioning system. While these beneficial effects were successfully evaluated, it is noted that in the absence of standard passive steel reinforcement and continuous bonding along the prestressing strands, all specimens ultimately failed in a brittle mode even though, at lower levels of prestress, specimens displayed noticeable ductility. These comments should be viewed in light of the fact that the span-to-depth ratio of specimens tested in this program was quite low and consequently had a high degree of shear behavior involved in the failure modes (shear deformation is much greater than bending deformation for depth beam or low span-to-depth ratio).

Strain gauge rosettes applied on the external surface of specimens were used to investigate stress distributions as prestressing and subsequent load applications were applied. During incremental prestressing procedures, stress distributions and principal stress axis directions varied due to sequential post-tensioning. Once

prestressing was completed in all strands, stress distributions appeared to be more uniform and maximum principal stress axes were aligned as expected. During the subsequent loading stage, principal directions varied between 25° and 35° to the longitudinal axis.

3.3.5 Deflections

As expected, the use of a spiral post-tensioning system resulted in mid-span deflections being considerably decreased by increasing levels of prestress. Most notably, referring to specimens H2 and HC1, the use, at the same prestress level, of a spiral post-tensioning system as opposed to a longitudinally aligned system of tendons resulted in a 38 percent decrease in deflection. The crack pattern is shown in Figure 3.28.
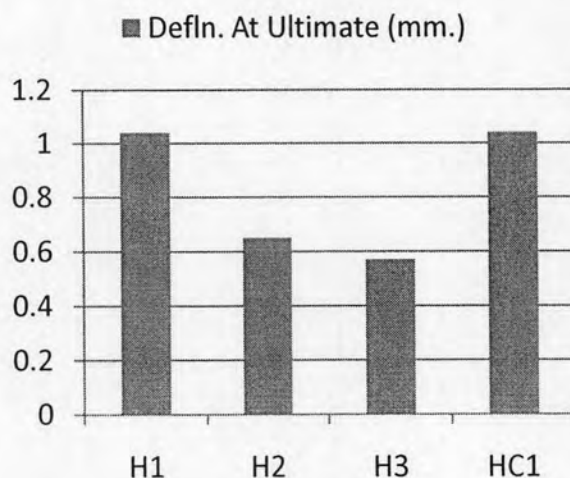

Figure 3.23 Deflection at ultimate

3.4 Discussion

A 3D finite element analysis (FEA) was performed using concrete plastic model to simulate effects of confinement behavior of concrete material, combined stress behavior while post crack behavior. The finite element modeling is illustrated in Figure 3.24.
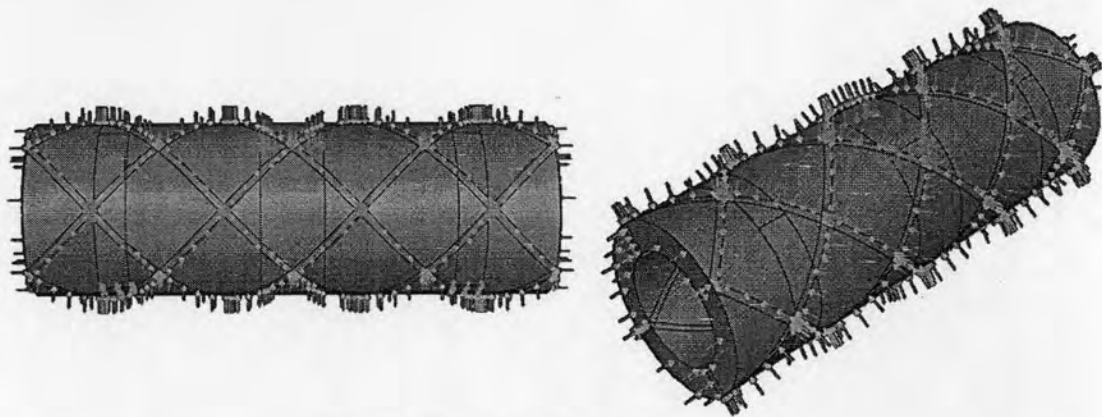
Figure 3.24 Finite element modeling

The model was simplified to investigate the effects of confinement in accounting for concrete plastic material behavior under simple confining represented as pressure loads along the strands aligned on the outside surface of concrete the thick-walled concrete pipe as illustrated in Figure 3.23. The magnitudes of pressure loads can be calculated as shown in equation (2.9) to (2.14) and are assumed to be averaged as uniform pressure all over the specimens as shown in Figure 2.2.

The uniaxial stress-strain relation for concrete was determined experimentally from cylinder compression tests and beam tension tests as shown in Figure 3.7 and Table 3.2.

The results from the finite element analysis were plotted and compared to the experimental results as shown in Figure 3.25. Stiffnesses in the elastic range from the finite element analysis results are similar since the plastic response was not included at that point. The stiffness of all specimens corresponded to the initial tangent modulus of elasticity, E_t. As plastic response is approached the concrete began to yield and the confining stress began to take an action and thus affected the stiffnesses of the specimens.
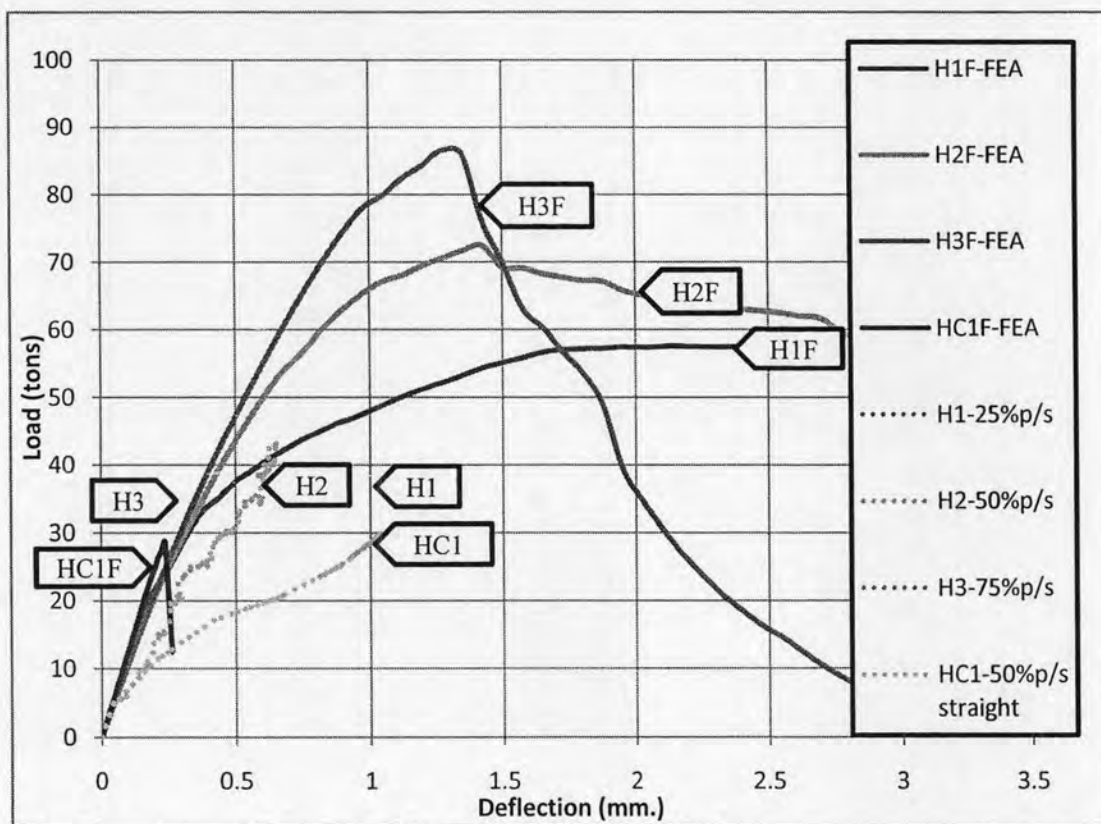
Figure 3.25 Load vs. deflection curves

First crack from FEA was predicted as shown in Figure 3.26. All specimens crack at bottom of mid-span according to bending stress. After concrete cracked, arch action was investigated as shown in Figure 3.27.
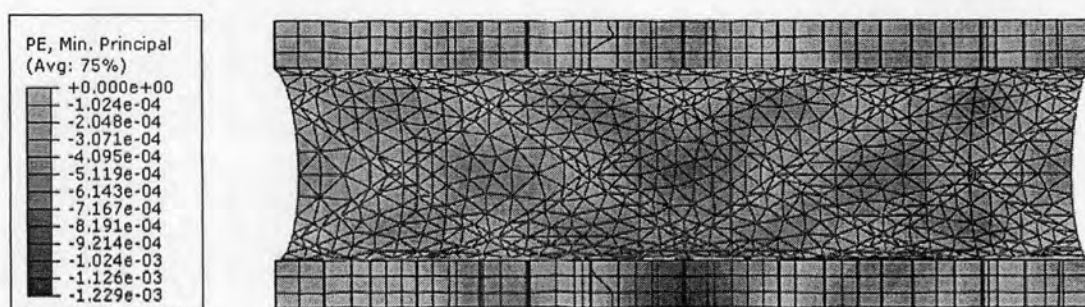

Figure 3.26 First crack prediction by FEM

S, Max. Principal
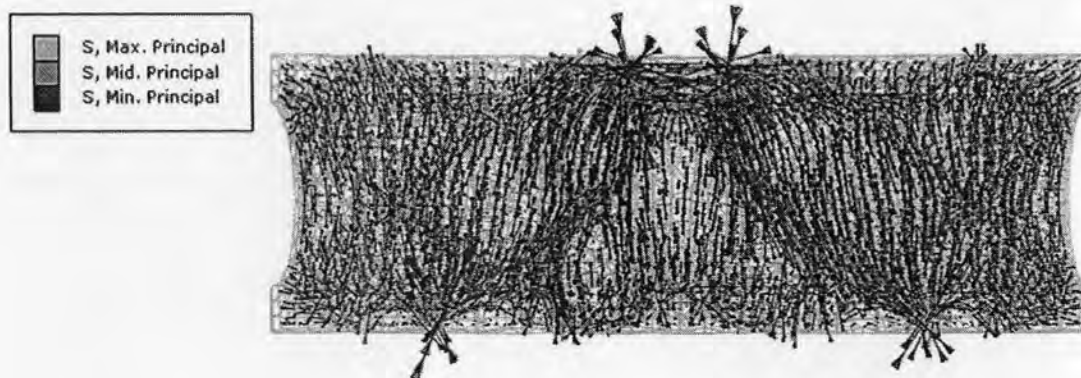S, Mid. Principal
S, Min. Principal

Figure 3.27 Principal stress distribution

The significant deviations of test predictions above actual test results are due to premature local concrete failure caused by the intense localized pressures exerted by the prestressing cables on the concrete. This effect could not be adequately modeled by the finite element model.

It should be noted that the laboratory tests did not represent the direct response to axial load of the active confinement of the spiral post-tensioning system. The tests performed represented indirect evaluation of active confinement behavior by subjecting simply-supported beam specimens to mid-span point loading. Due to the limitation of specimen size and loading equipment, direct axial compression tests on cylindrical concrete members could not be performed. However, evaluation of the beneficial confinement and shear strength enhancement of spiral prestressing strands was validated.

The finite element analysis results failed to correspond favorably with test results. This was due to the complex overlapping stress fields in the specimens as well as to the highly localized and intense stresses between the tendons and the concrete. Additionally, these stresses increased with applied loading and resulted in localized failure along the tendons. This local failure phenomenon was noted for all specimens.

General observations reveal that the ultimate strength results from finite element analysis and those from the experimental results increase correspondingly with increased levels of confining prestress. As pointed out, however, the ultimate

strength values of theoretical and experimental results do not correspond well due to local failure phenomena. Stress field overlapping, and non-compliant assumptions of modeling.

3.5 Summary

This dissertation focuses on active confinement provided by spiral post-tensioning systems applied to structural concrete materials. This study was simplified to reduce any unexpected complexity and to emphasize behavior of confined and loaded concrete regions. The interaction between prestressing tendons and concrete was interpreted as loading on the exterior surface of the concrete along the lines of prestressing tendons. It was indicated that prestress losses due to friction and anchorage take-up compensated each other and were assumed to be uniform throughout the prestressed strand as illustrated in Figure 2.2. Other losses such as creep loss, shrinkage loss and steel relaxation that gradually became distributed all along the length of prestress strands were considered and additional prestress force was applied from the jacking stage to offset those losses.

Stress changes in strands due to load application were neglected according to small deformation assumptions and levels of initial prestress in the strands. Higher initial prestress force cause lower percentage of differences to the stress in strands due to load.

Direct axial compressive strength tests to evaluate confinement effects could not be performed due to unavailability of high capacity loading equipment required and the limitation of specimen size. Test specimens were mounted as simply support beams and point-loaded at mid-span. Furthermore, specimens were designed as thick-walled pipe to reduce shear capacity. Although this experimental study did not directly indicate the effects of active confinement provided by spiral post-tensioning systems for axially loaded specimens, the results do show how specimen strength and ductility under shear and moment are improved significantly. The results have demonstrated the beneficial aspects of spiral post-tensioning of circular members

subjected to shear and bending. This is a more rigorous test of the system than would be the case if such members were simply loaded under axial compression.

Due to the complexity of combined stresses due to prestress forces and short-span loading test specimens were setup to evaluate these effects.

Losses due to prestress were taken into account by increasing jacking forces accordingly to offset loss effects. During post-tensioning a sequential prestressing procedure was strictly followed to avoid accidental failure caused by imbalances of torsional-bending stresses between tendons. Applying prestress simultaneously to counterbalancing pairs of clockwise versus counter-clockwise strands is, in general, suggested for the construction sequence.

According to the experimental results, all specimens failed in brittle mode because of the prestress tendons are unbonded type and spacing of prestress tendons indicated by the ratios s/D, which was 0.56 for the specimens tested, was determined to be too high for developing ductile behavior. Referring to the study of Shamim A. Sheikh and Murat T. Toklucu (1993), for ductile behavior, s/D ratios should no greater than 0.24. Principal stress directions at the middle of specimen depths varied between 25° and 35° to the longitudinal axis as the result of combined shear stress from loading and pre-compression stress from prestressing. Stiffness of the specimens increased proportionally to the levels of prestress. First cracking occurred near mid-span at the bottom of all specimens. Cracking strength and ultimate strength increased proportionally with the levels of prestress. Comparing specimen H2 to the control specimen (HC1) with straight tendons having the same level of prestress, cracking strength and ultimate strength of specimen H2 were dramatically higher than those of the control specimen HC1, being about 41% and 45% higher, respectively.

While finite element analysis was useful for determining the overall behavior of test specimens, predicted results for ultimate strength of test specimens were highly overestimated. The method, however, was capable of representing the effects of active confinement, deep beam action, and combined stresses due to prestressing and loading. A comparison of finite element results to the finite difference results

that base on bending theory with assumed confined concrete model showed that both methods made similar predictions as shown in Table 3.6 except specimen HC1 that FEM result is different to FDM result according to shear effect and arch action. Furthermore, by the effect of shear and arch action, FEM result of specimen HC1 is also close to the experimental result. The main reason for the discrepancy between the predicted ultimate strengths of specimens using finite elements is related to the localized failure of the concrete before the strength reach overall failure. As a result the concrete failed along the tendons due to a complex localized stress field in the contact zone.
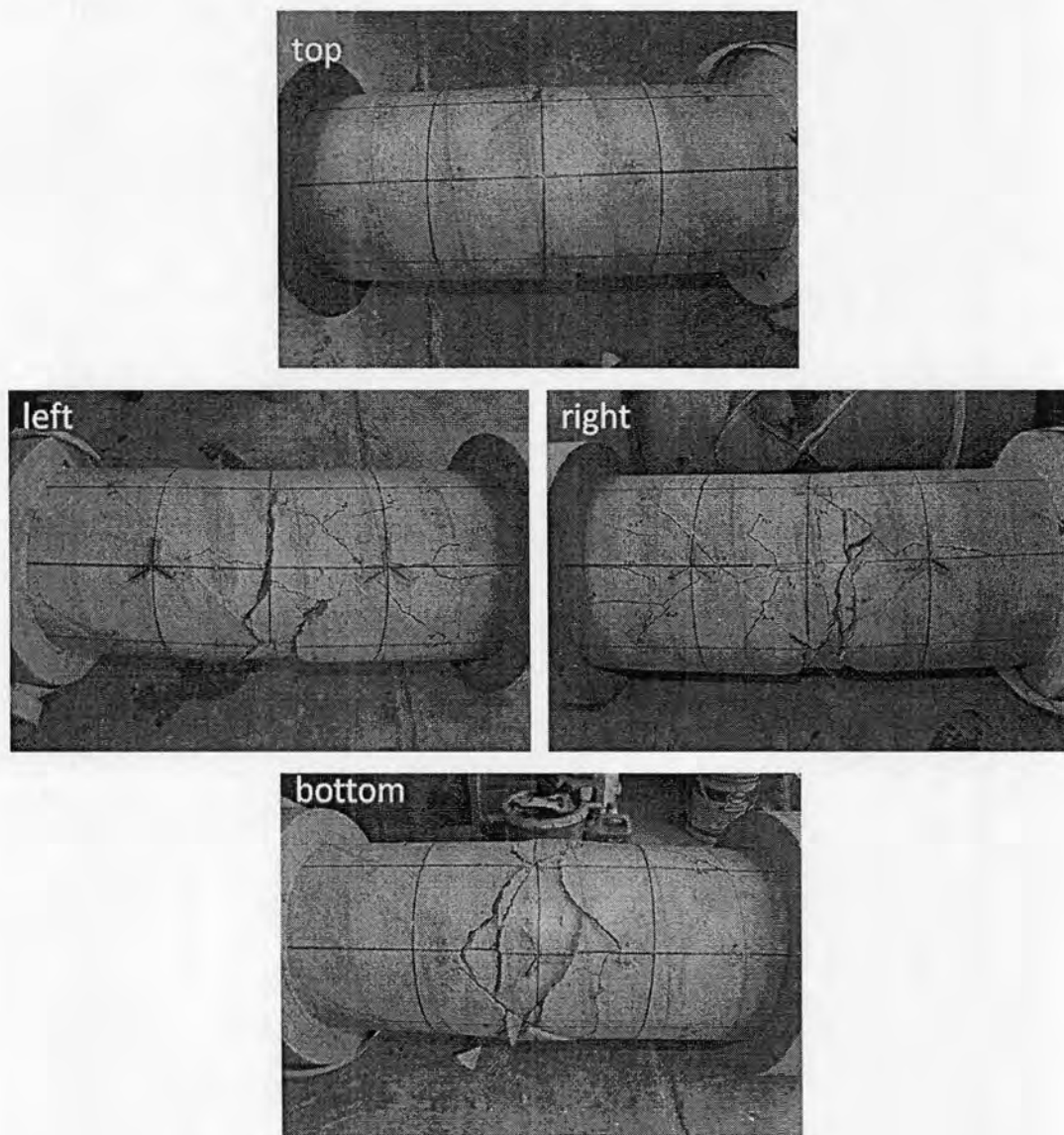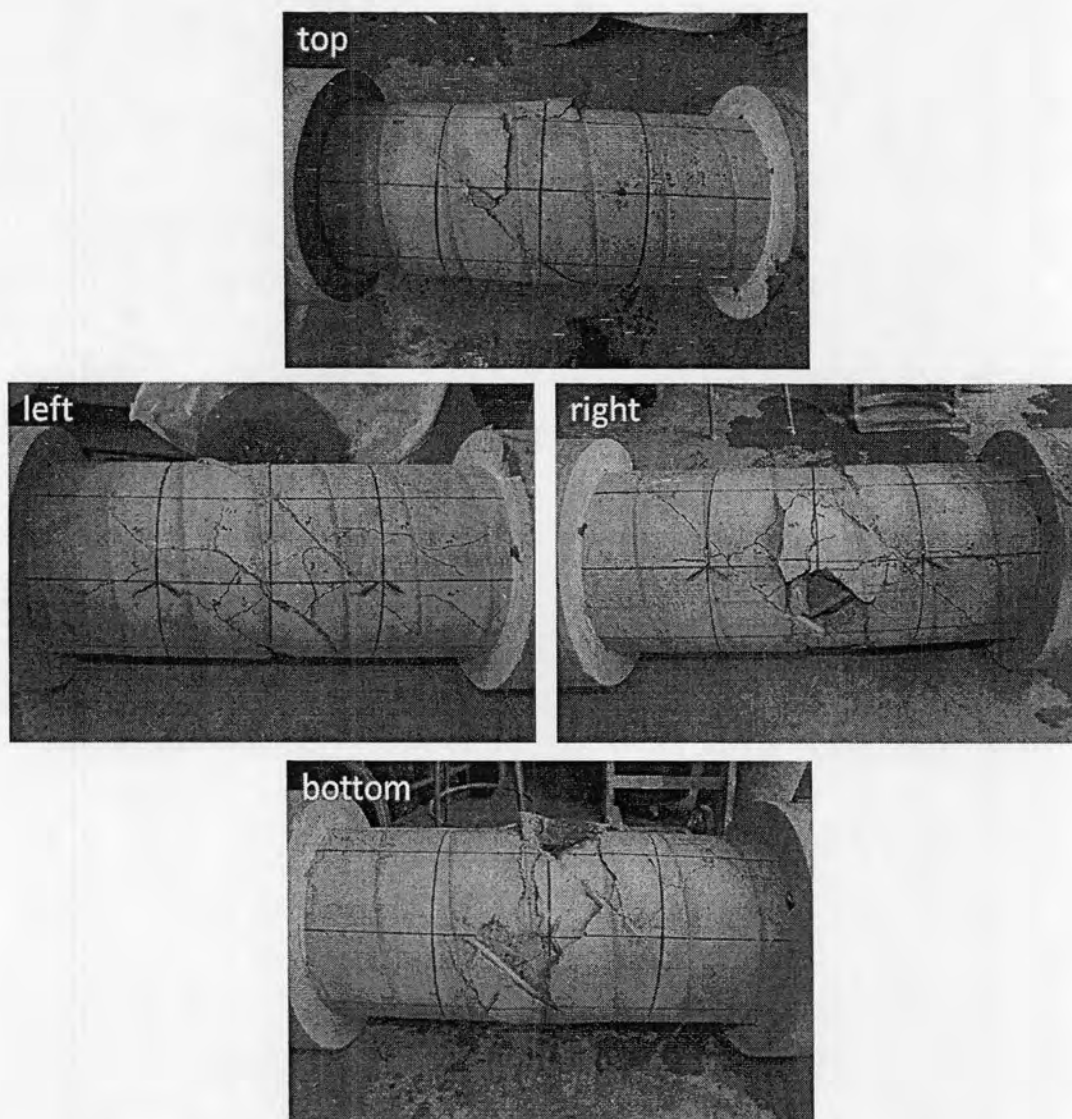

Figure 3.28a Cracked pattern of specimen H1

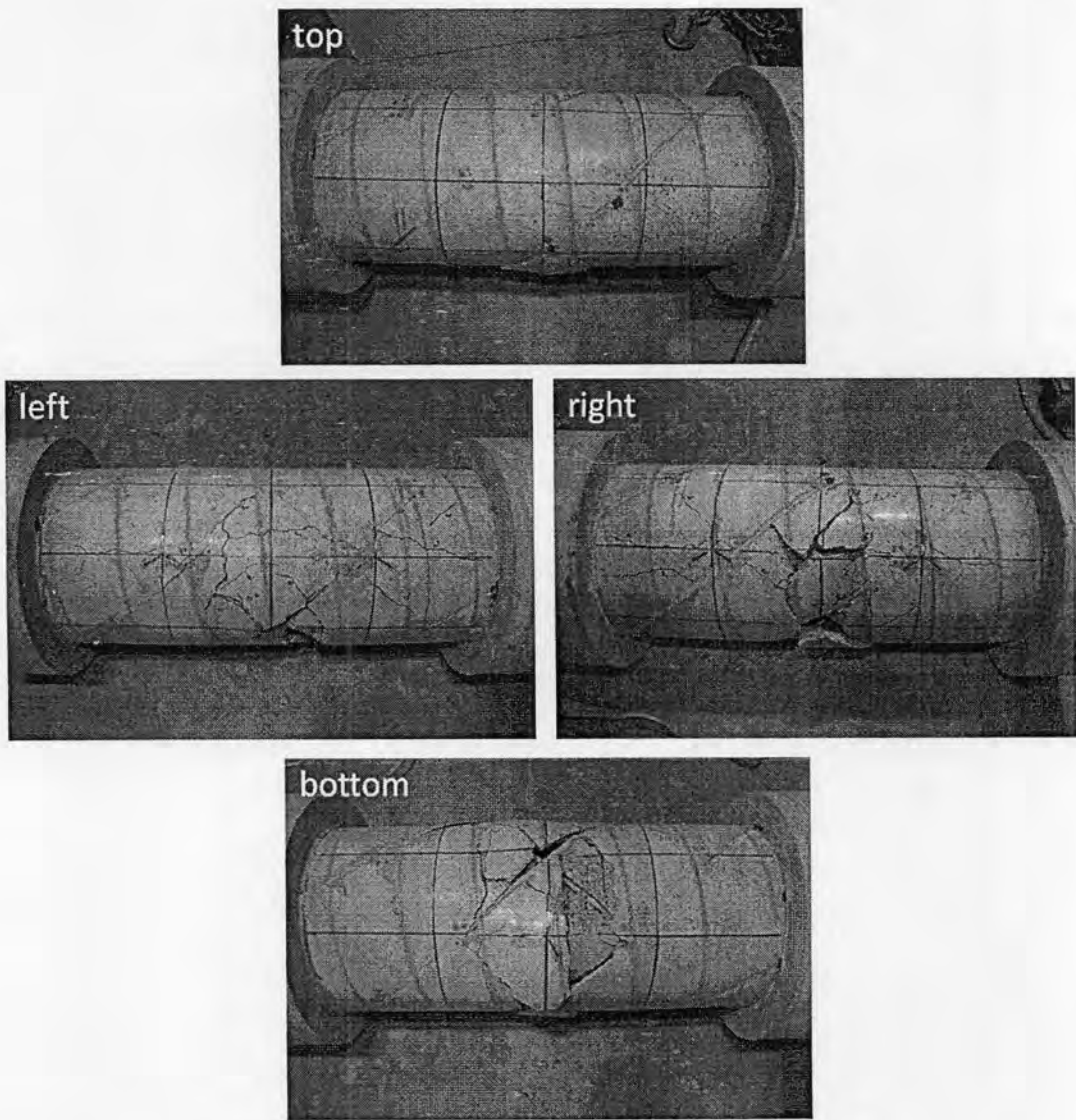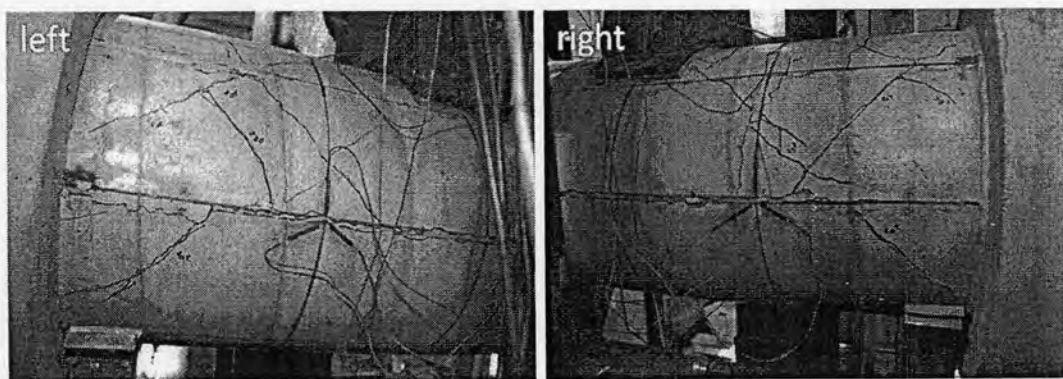Figure 3.28b Cracked pattern of specimen H2

Figure 3.28c Cracked pattern of specimen H3

Figure 3.28d Cracked pattern of specimen HC1